

SARS-CoV-2 entry into human airway organoids is serine protease-mediated and facilitated by the multibasic cleavage site

Anna Z Mykytyn^{1†}, Tim I Breugem^{1†}, Samra Riesebosch¹, Debby Schipper¹, Petra B van den Doel¹, Robbert J Rottier², Mart M Lamers^{1‡}, Bart L Haagmans^{1‡*}

¹Viroscience Department, Erasmus University Medical Center, Rotterdam, Netherlands; ²Department of Pediatric Surgery, Erasmus University Medical Center - Sophia Children's Hospital, Rotterdam, Netherlands

Abstract Coronavirus entry is mediated by the spike protein that binds the receptor and mediates fusion after cleavage by host proteases. The proteases that mediate entry differ between cell lines, and it is currently unclear which proteases are relevant *in vivo*. A remarkable feature of the severe acute respiratory syndrome coronavirus 2 (SARS-CoV-2) spike is the presence of a multibasic cleavage site (MBCS), which is absent in the SARS-CoV spike. Here, we report that the SARS-CoV-2 spike MBCS increases infectivity on human airway organoids (hAOs). Compared with SARS-CoV, SARS-CoV-2 entered faster into Calu-3 cells and, more frequently, formed syncytia in hAOs. Moreover, the MBCS increased entry speed and plasma membrane serine protease usage relative to cathepsin-mediated endosomal entry. Blocking serine proteases, but not cathepsins, effectively inhibited SARS-CoV-2 entry and replication in hAOs. Our findings demonstrate that SARS-CoV-2 enters relevant airway cells using serine proteases, and suggest that the MBCS is an adaptation to this viral entry strategy.

*For correspondence:
b.haagmans@erasmusmc.nl

†These authors contributed equally to this work

‡These authors also contributed equally to this work

Competing interests: The authors declare that no competing interests exist.

Funding: See page 20

Received: 31 October 2020

Accepted: 31 December 2020

Published: 04 January 2021

Reviewing editor: Mark Marsh, University College London, United Kingdom

© Copyright Mykytyn et al. This article is distributed under the terms of the [Creative Commons Attribution License](https://creativecommons.org/licenses/by/4.0/), which permits unrestricted use and redistribution provided that the original author and source are credited.

Introduction

The ongoing coronavirus disease (COVID-19) pandemic is caused by the severe acute respiratory syndrome coronavirus 2 (SARS-CoV-2), which emerged in central China late 2019 (Zhu et al., 2020). Within months, this virus spread globally, and as of October 15, 2020, over 38 million cases have been reported, including over 1 million deaths. Halting SARS-CoV-2 spread has shown to be highly complex, putting great strain on health systems globally. SARS-CoV-2 is the third zoonotic coronavirus to emerge from animal reservoirs within the past two decades, after SARS-CoV and Middle East respiratory syndrome coronavirus (MERS-CoV), in 2002 and 2012, respectively (Drosten et al., 2003; Kuiken et al., 2003; Peiris et al., 2003b; Zaki et al., 2012). In contrast to SARS-CoV-2, SARS-CoV and MERS-CoV have not attained sustained human-to-human transmission. These coronaviruses belong to the Betacoronavirus genus (family Coronaviridae, subfamily Orthocoronavirinae), which is thought to ultimately originate from bats, but can spread to humans via intermediate hosts (Hu et al., 2015; Lau et al., 2010; Wang et al., 2014).

Currently, it is largely unknown what factors determine coronavirus transmission to and between humans, but one important determinant may be the coronavirus spike (S) protein, which is the main glycoprotein incorporated into the viral envelope. Enveloped viruses, including coronaviruses, deposit their genomes into host cells by coalescing their membranes with the cell. This function is executed by S protein trimers, which fuse viral and cellular membranes after binding to the entry receptor (Hulswit et al., 2016). In addition, coronaviruses can spread from cell to cell when

coronavirus S proteins traffic to the plasma membrane of infected cells and fuse with neighboring cells, generating multinucleated giant cells (syncytia). Coronavirus S proteins are synthesized in infected cells in a stable and fusion-incompetent form and are activated through cleavage by host proteases. Proteolysis controls the timely release of the S protein's stored energy required to fuse membranes, which allows virions to be stable in the environment yet fusogenic after contacting entry receptors on host cell membranes.

Cleavage is essential for coronavirus infectivity and can occur in the secretory pathway of infected cells or during viral entry into target cells (*Hulswit et al., 2016; Millet and Whittaker, 2015*). Several groups of host proteases, including type II transmembrane serine proteases (hereafter referred to as serine proteases), proprotein convertases, and cathepsins, can cleave the S protein. Specific sites in the S protein regulate protease usage and therefore play an important role in determining cell tropism. Similarly, tropism can be determined by the availability of proteases that can activate the S protein (*Belouzard et al., 2012; Menachery et al., 2020; Millet and Whittaker, 2015; Yang et al., 2014; Yang et al., 2015*). The S protein consists of two domains, the receptor binding (S1) domain and the fusion (S2) domain. These domains are separated by the S1/S2 cleavage site, which in some coronaviruses, such as SARS-CoV-2, forms an exposed loop that harbors multiple arginine residues and is therefore referred to as a multibasic cleavage site (MBCS) (*Walls et al., 2020; Wrapp et al., 2020*). Cleavage of this site can occur in secretory systems of infected cells by proprotein convertases, including furin. S1/S2 cleavage does not directly trigger fusion but may facilitate or regulate further cleavage (*Park et al., 2016*). A second proteolysis step takes place at a more C-terminal site within the S2 domain, notably the S2' site. S2' cleavage is thought to occur after the virus has been released from producing cells and is bound to host cell receptors on receiving cells. The S2' site is processed by serine proteases on the plasma membrane or by cathepsins in the endosome. Whereas S2' cleavage appears to be crucial for coronavirus infectivity, not all coronaviruses contain a multibasic S1/S2 site and little is known of its function (*Hulswit et al., 2016*). Until recently, all viruses within the clade of SARS-related viruses, including SARS-CoV, were found to lack a multibasic S1/S2 cleavage site. However, SARS-CoV-2 contains a proline-arginine-arginine-alanine (PRRA) insertion into the S protein, precisely N-terminally from a conserved arginine, creating a multibasic RRAR cleavage motif. Exchanging the SARS-CoV-2 S MBCS for the SARS-CoV monobasic site was recently shown to decrease fusogenicity on a monkey kidney cell line (VeroE6) and infectivity in a human lung adenocarcinoma cell line (Calu-3) (*Hoffmann et al., 2020a; Shang et al., 2020*). However, cancer cells often poorly represent untransformed cells and thus the question remains whether the MBCS would affect infectivity on relevant airway cells. Another study showed that entry of SARS-CoV-2 pseudoparticles (PP) into Calu-3 cells could be blocked using a clinically approved serine protease inhibitor (camostat mesylate) (*Hoffmann et al., 2020b*). In contrast, in most other cell lines (including the lung cell line A549), recent CRISPR-Cas9 screens have suggested that SARS-CoV-2 entry in cell lines appears to be mediated by endosomal cathepsins (*Daniloski et al., 2020; Wei et al., 2020a*). These discrepancies between human lung cell lines underscore the importance of using relevant cells, such as human airway organoids (hAOs), to study SARS-CoV-2 entry. Here, we investigated if the SARS-CoV-2 MBCS affects entry into relevant human airway cells (1), if the MBCS can alter protease usage during entry (2), and which entry pathway is taken by SARS-CoV-2 in hAOs (3).

Results

Entry into lung adenocarcinoma cells and hAOs is facilitated by the SARS-CoV-2 S MBCS

Recently, *Hoffmann et al., 2020a* showed that the SARS-CoV-2 multibasic cleavage motif increases entry into Calu-3 cells by exchanging this motif and several N-terminally flanking amino acids with the monobasic S1/S2 site found in SARS-CoV or in a related bat virus RaTG13 (*Hoffmann et al., 2020a*). Building on these observations, we generated several SARS-CoV-2 S protein mutants and used these to generate vesicular stomatitis virus (VSV)-based PP stocks expressing a green fluorescent protein (GFP). Instead of exchanging cleavage sites, we mutated the minimal RXXR multibasic cleavage motif by deleting the PRRA insertion (Del-PRRA), changing the last arginine to an alanine (R685A) or to a histidine (R685H) in order to preserve the positive charge at this site (**Figure 1A**).

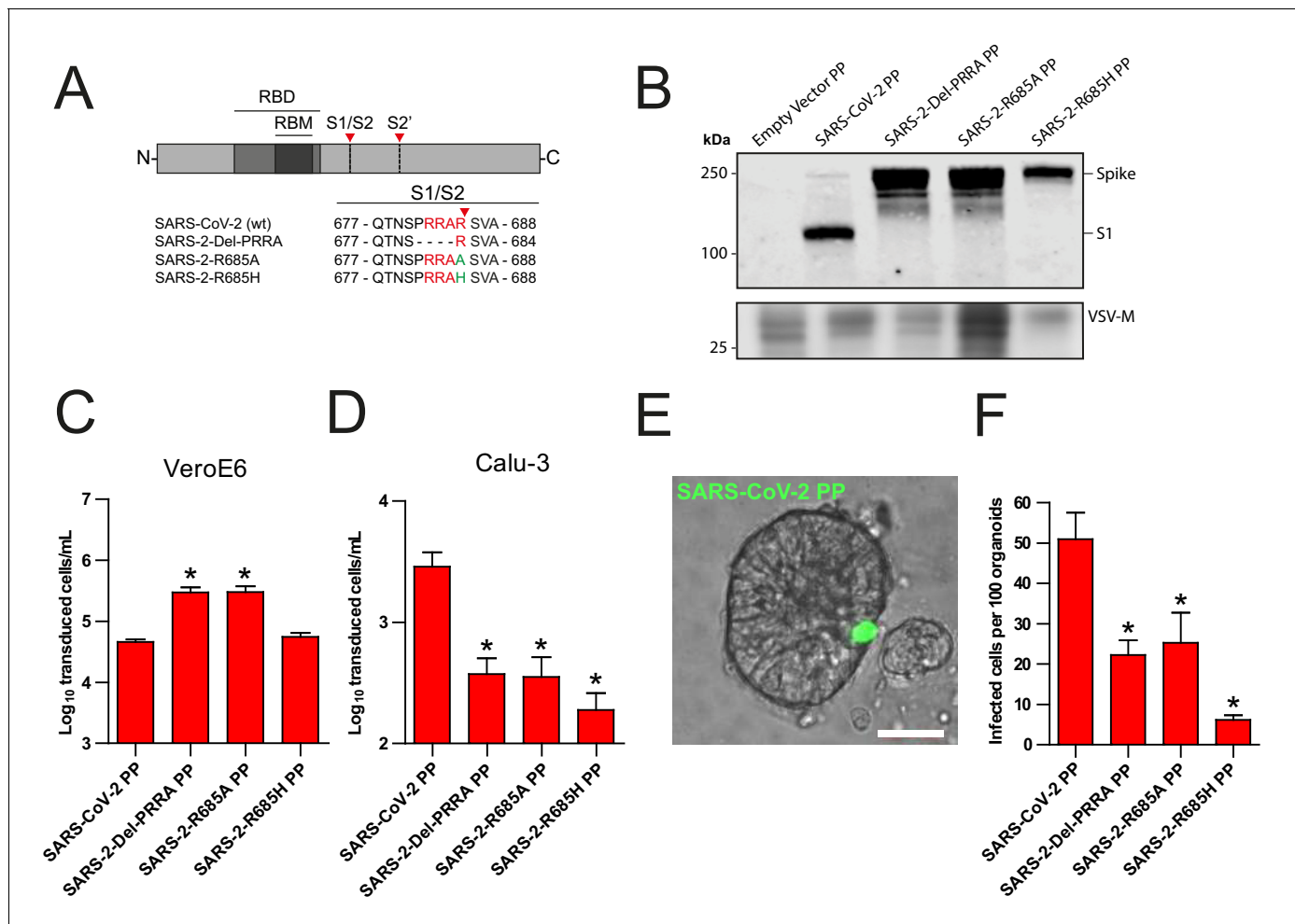


Figure 1. The SARS-CoV-2 S multibasic cleavage site mediates entry into human airway organoids. (A) Schematic overview of SARS-CoV-2 S protein mutants. MBCS residues are indicated in red; amino acid substitutions are indicated in green. Red arrows indicate cleavage sites. The SARS-CoV-2 S MBCS was mutated to either remove the PRRA motif (SARS-2-Del-PRRA) or substitute the R685 site (SARS-2-R685A and R685H). (B) Comparison of S cleavage of SARS-CoV-2 PPs and the MBCS mutants. Western blots were performed against S1 with VSV-M silver stains as a production control. (C and D) PP infectivity of SARS-CoV-2 S and MBCS mutants on VeroE6 (C) and Calu-3 (D) cells. (E) Differentiated hAO cultures were infected with concentrated SARS-CoV-2 PPs containing a GFP reporter, indicated in green. Scale bar indicates 20 μ m. (F) SARS-CoV-2 PP and MBCS mutant infectivity on bronchiolar hAO cultures. One-way ANOVA was performed for statistical analysis comparing all groups with SARS-CoV-2 PPs. Experiments were performed in triplicate (B and D, F). Representative experiments from at least two independent experiments are shown (C and D). Combined data from three independent experiments is shown (F). Error bars indicate SEM. * $p < 0.05$. GFP, green fluorescent protein; hAO, human airway organoid; MBCS, multibasic cleavage site; PP, pseudoparticles; RBD, receptor binding domain; RBM, receptor binding motif. The online version of this article includes the following figure supplement(s) for figure 1:

Figure supplement 1. hAO cultures grown at 2D air-liquid interface are well-differentiated and express ACE2 and TMPRSS2.

Immunoblotting revealed that wild-type and mutant PPs were produced at similar levels (Figure 1B). S1/S2 cleavage was observed for the wild-type SARS-CoV-2 PPs and abrogated by the PRRA deletion and the R685A and R685H substitutions, which is in agreement with studies showing that the SARS-CoV-2 S is cleaved by proprotein convertases, possibly furin (Hoffmann et al., 2020a; Shang et al., 2020). Next, we assessed the infectivity of these viruses and found that the SARS-2-Del-PRRA and SARS-2-R685A mutants were 5- to 10-fold more infectious on VeroE6 cells (Figure 1C). In contrast, on the lung adenocarcinoma cell line Calu-3, the SARS-2-Del-PRRA, SARS-2-R685A, and SARS-2-R685H PPs were approximately 5- to 10-fold less infectious compared with the wild-type PPs (Figure 1D). These data show that the PRRA deletion and single point mutations could functionally destroy the MBCS and suggest that this site enhances airway cell entry. Next, we assessed the effect of the MBCS in a relevant cell culture system. A 3D airway organoid model that

allows efficient SARS-CoV-2 replication where infectious virus titers increase over time has not yet been established, but we previously reported that 2D airway organoid-derived air-liquid interface differentiated cultures allow efficient SARS-CoV-2 replication (Lamers *et al.*, 2020). In this model, hAOs (Sachs *et al.*, 2019) are dissociated, seeded onto collagen-coated Transwell inserts, and differentiated at air-liquid interface in Pneumacult ALI medium (Stemcell). After differentiation, cultures contain ciliated cells, club cells, and goblet cells (Figure 1—figure supplement 1). Moreover, they express the SARS-CoV-2 entry receptor angiotensin-converting enzyme 2 (ACE2) and transmembrane protease serine 2 (TMPRSS2), a serine protease previously shown to mediate SARS-CoV-2 entry when overexpressed (Figure 1—figure supplement 1D,E; Hoffmann *et al.*, 2020b). To set up a 3D model, we dissociated these 2D air-liquid differentiated cultures into small clumps, infected these in suspension, and then re-plated the clumps into basement membrane extract (BME), in which they formed spheroids. SARS-CoV-2 PPs successfully infected these hAOs, as observed by fluorescent microscopy (Figure 1E). SARS-CoV-2 PPs were approximately two times more infectious on these cells compared with the SARS-2-Del-PRRA and SARS-2-R685A mutants, and eight times more infectious than the SARS-2-R685H mutant (Figure 1F), demonstrating that the SARS-CoV-2 MBCS facilitates entry into human airway cells.

SARS-CoV-2 enters Calu-3 cells faster than SARS-CoV and entry speed is increased by the MBCS

As SARS-CoV lacks the MBCS, we compared its infectivity to SARS-CoV-2 and found that both PPs readily infected Calu-3 cells, indicating that the SARS-CoV S has adaptations other than the MBCS to facilitate airway cell infection (Figure 2A). Likewise, inserting the PRRA motif into SARS-CoV S and thereby generating an MBCS did not increase PP infectivity on Calu-3 cells (Figure 2—figure supplement 1). To investigate this further, we compared the entry route taken by these viruses in Calu-3 cells. For this purpose, we used inhibitors of two major coronavirus entry pathways (Hulswit *et al.*, 2016). Serine proteases are known to mediate early coronavirus entry on the plasma membrane or in the early endosome, whereas cathepsins facilitate entry in late, acidified endosomes. Concentration ranges of either a serine protease inhibitor (camostat mesylate; hereafter referred to as camostat) or a cathepsin inhibitor (E64D) were used to assess the entry route into Calu-3 cells. Entry of SARS-CoV-2 PPs was not inhibited by E64D, but could be inhibited by camostat, indicating that SARS-CoV-2 exclusively uses serine proteases for entry into these cells (Figure 2B,C). For SARS-CoV PPs, entry was inhibited slightly by E64D (~10%), but camostat had a far stronger effect (~90%), indicating that SARS-CoV mainly uses serine proteases to enter Calu-3 cells but that a small fraction of virions enter via cathepsins (Figure 2B,C). Previously, Calu-3 cells have been suggested to have low levels of cathepsin activity (Park *et al.*, 2016). The observation that some SARS-CoV PPs use cathepsins suggests that this virus less efficiently uses the surface serine proteases encountered early during entry, resulting in particles accumulating in the endosome, where they are cleaved by cathepsins. To test this, we measured the serine protease-mediated entry rate of SARS-CoV-2 and SARS-CoV by blocking entry on Calu-3 cells at different time points postinfection using camostat. Cells were pretreated with E64D to prevent any cathepsin-mediated entry. Using both PPs and authentic virus (Figure 2D,E), we observed that SARS-CoV-2 entered faster than SARS-CoV via serine proteases. Next, we assessed whether the presence of an MBCS could increase the serine protease-mediated entry rate into Calu-3 cells. For this purpose, we used SARS-CoV S PPs containing the PRRA insertion (SARS-PRRA) (Figure 2F). Immunoblotting revealed that, in contrast to SARS-CoV PPs, SARS-PRRA PPs were partially cleaved (Figure 2G). Whereas wild-type SARS-CoV PPs used cathepsins, SARS-PRRA PPs did not (Figure 2H,I). The serine protease-mediated entry rate of SARS-PRRA PPs on Calu-3 cells was higher compared with SARS-CoV PPs (Figure 2J), and it was lower for SARS-2-Del-PRRA PPs compared with SARS-CoV-2 PPs (Figure 2K). These findings show that the SARS-CoV-2 MBCS facilitates serine protease-mediated entry on Calu-3 cells.

Cell-cell fusion is facilitated by the SARS-CoV-2 MBCS and SARS-CoV-2 is more fusogenic than SARS-CoV on hAOs

Next, we used a GFP complementation cell-cell fusion assay (Figure 3—figure supplement 1A,B) to determine whether entry rate was associated with fusogenicity. In this assay, S and GFP-11 co-

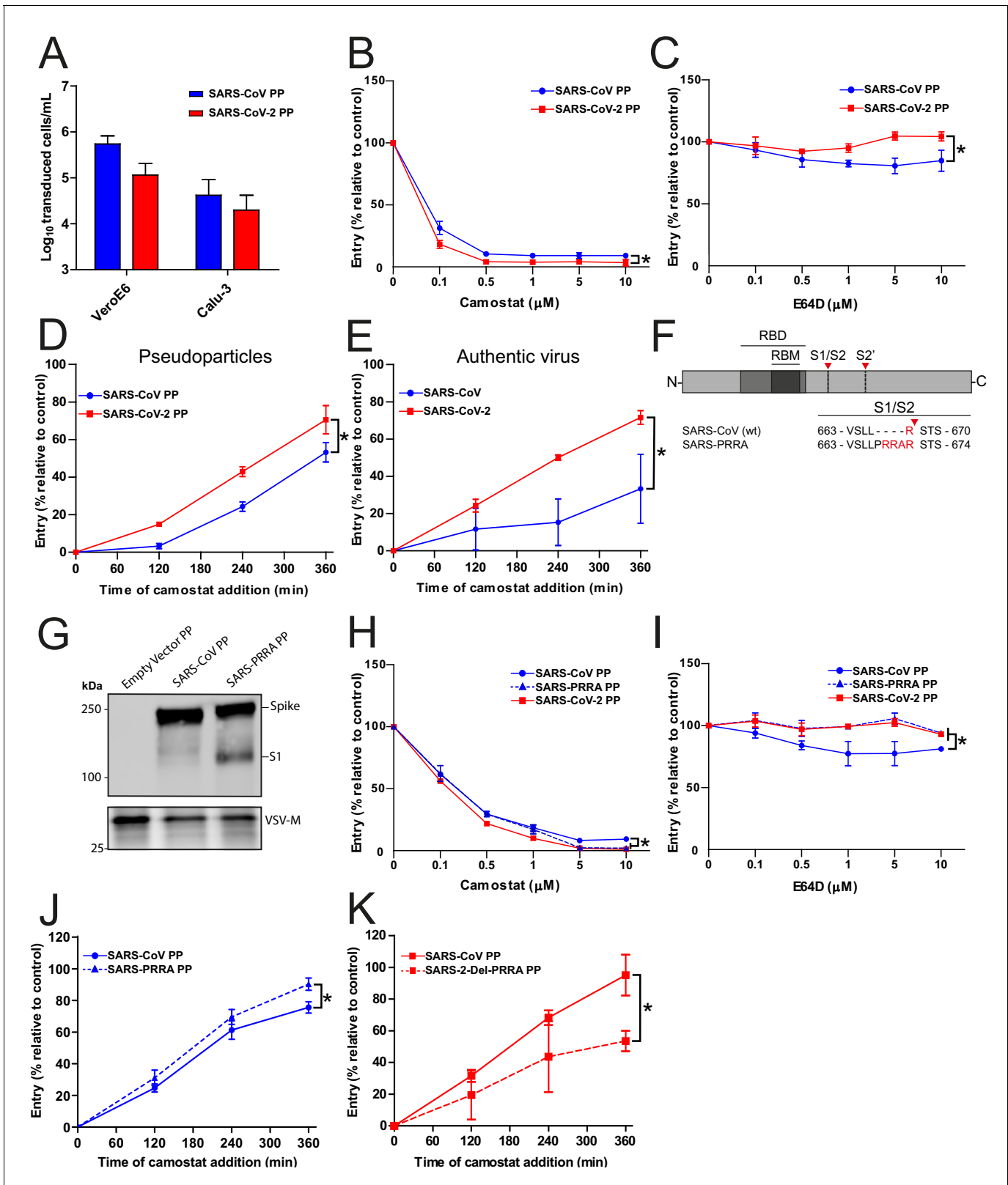


Figure 2. SARS-CoV-2 enters faster on Calu-3 cells than SARS-CoV and entry speed is increased by the multibasic cleavage site. (A) SARS-CoV PP and SARS-CoV-2 PP infectivity on VeroE6 and Calu-3 cells. (B and C) SARS-CoV PP and SARS-CoV-2 PP entry route on Calu-3 cells. Cells were pretreated with a concentration range of camostat (B) or E64D (C) to inhibit serine proteases and cathepsins, respectively. T-test was performed for statistical analysis at the highest concentration. * $p < 0.05$. (D and E) SARS-CoV PP, SARS-CoV-2 PP (D) and authentic virus (E) entry speed on Calu-3 cells. T-test

Figure 2 continued on next page

Figure 2 continued

was performed for statistical analysis at the latest time point. * $p < 0.05$. (F) Schematic overview of SARS-CoV S protein mutants. MBCS residues are indicated in red. The SARS-CoV-2 PRRA motif was inserted into SARS-CoV PPs (SARS-PRRA). (G) Comparison of S1 cleavage of SARS-CoV PP and the MBCS mutant. VSV-M silver stains are shown as a production control. (H and I) SARS-CoV PP, SARS-PRRA PP, and SARS-CoV-2 PP entry route on Calu-3 cells. Cells were pretreated with a concentration range of camostat (H) or E64D (I) to inhibit plasma membrane and endosomal entry, respectively. One-way ANOVA was performed for statistical analysis comparing all groups with SARS-CoV PPs at the highest concentration. * $p < 0.05$. (J and K) Entry speed on Calu-3 cells of SARS-CoV PPs compared with SARS-PRRA PPs (J) and SARS-CoV-2 PPs compared with SARS-2-Del-PRRA PPs (K). T-test was performed for statistical analysis at the latest time point. * $p < 0.05$. Experiments were performed in triplicate (A–E, H–K). Representative experiments from at least two independent experiments are shown. Error bars indicate SD. ANOVA, analysis of variance; MBCS, multibasic cleavage site; PP, pseudoparticles.

The online version of this article includes the following figure supplement(s) for figure 2:

Figure supplement 1. SARS-CoV PP infectivity into Calu-3 cells is not altered by the insertion of the multibasic cleavage site.

transfected HEK-293T cells fuse with GFP1-10 expressing Calu-3 cells, resulting in GFP complementation and fluorescence. In HEK-293T cells, MBCS containing S proteins were more cleaved than S proteins without this site (**Figure 3A**). We observed that SARS-CoV-2 S was more fusogenic than SARS-CoV S on Calu-3 cells (**Figure 3B,C**), VeroE6 cells, and VeroE6-TMPRSS2 cells (**Figure 3—figure supplement 1C–D and E–F**). The expression of TMPRSS2 increased fusion about twofold for both S proteins (**Figure 3—figure supplement 1G**). The insertion of the MBCS into SARS-CoV S increased fusion, whereas mutations in the SARS-CoV-2 S MBCS decreased fusion (**Figure 3B,C**). To investigate differences in fusogenicity in a relevant cell system, we infected 2D differentiated hAO air–liquid interface cultures with SARS-CoV-2 and SARS-CoV and assessed the formation of syncytial cells at 72 hr postinfection using confocal microscopy. Cells were termed syncytial cells when at least two nuclei were present within a single viral antigen-positive cell that lacked demarcating tight junctions. SARS-CoV-2 frequently induced syncytia, whereas SARS-CoV-infected cells rarely contained multiple nuclei (**Figure 3D,E** for quantification).

The SARS-CoV-2 MBCS increases serine protease usage and decreases cathepsin usage

The findings above indicate that SARS-CoV-2 S is more fusogenic and mediates faster entry through serine proteases compared with SARS-CoV, indicating that the MBCS alters protease usage. To investigate this, cells that contain both serine and cathepsin protease-mediated entry should be used. Therefore, we focused on VeroE6 cells, which have an active cathepsin-mediated cell entry pathway, as on these cells both SARS-CoV-2 PP and SARS-CoV PP entry was inhibited by E64D, and not by camostat (**Figure 4A,B**). To generate a cell line in which both entry pathways are active, we stably expressed TMPRSS2 in VeroE6 cells. In these cells, SARS-CoV-2 PP entry was inhibited ~95% by camostat, whereas SARS-CoV PPs were only inhibited ~35% (**Figure 4C,D**). In accordance, E64D did not block SARS-CoV-2 PP entry, while it decreased SARS-CoV PP entry ~30%. These findings indicate that despite a functional serine protease-mediated entry pathway, a significant part of SARS-CoV PPs still retained cathepsin-mediated entry, whereas SARS-CoV-2 PPs only used serine proteases for entry. This phenotype was found to be linked to the MBCS as SARS-CoV-2 PPs containing mutations in this site entered less through serine proteases and more through cathepsins (**Figure 4E,F**). In accordance, the introduction of the MBCS into SARS-CoV PPs increased serine protease usage, while decreasing cathepsin usage (**Figure 4G,H**).

SARS-CoV-2 entry and replication are dependent on serine proteases in hAOs

Altogether, our findings show that SARS-CoV-2 preferentially uses serine proteases for entry, when present, and that the MBCS increases fusogenicity and infection of human airway cells. Hence, serine protease inhibition could be an attractive therapeutic option. Therefore, we assessed whether camostat could block SARS-CoV-2 entry and replication using hAOs. In these differentiated organoids the apical side of the cells was facing outwards (**Figure 5A,B**), facilitating virus excretion into the culture medium. These cells were infected with SARS-CoV-2 at a high multiplicity of infection (MOI) of 2, but pretreatment with camostat efficiently blocked virus infection as evidenced by confocal microscopy on hAOs fixed at 16 hr postinfection (**Figure 5A**). Cathepsin inhibition did not affect entry. At 24 hr

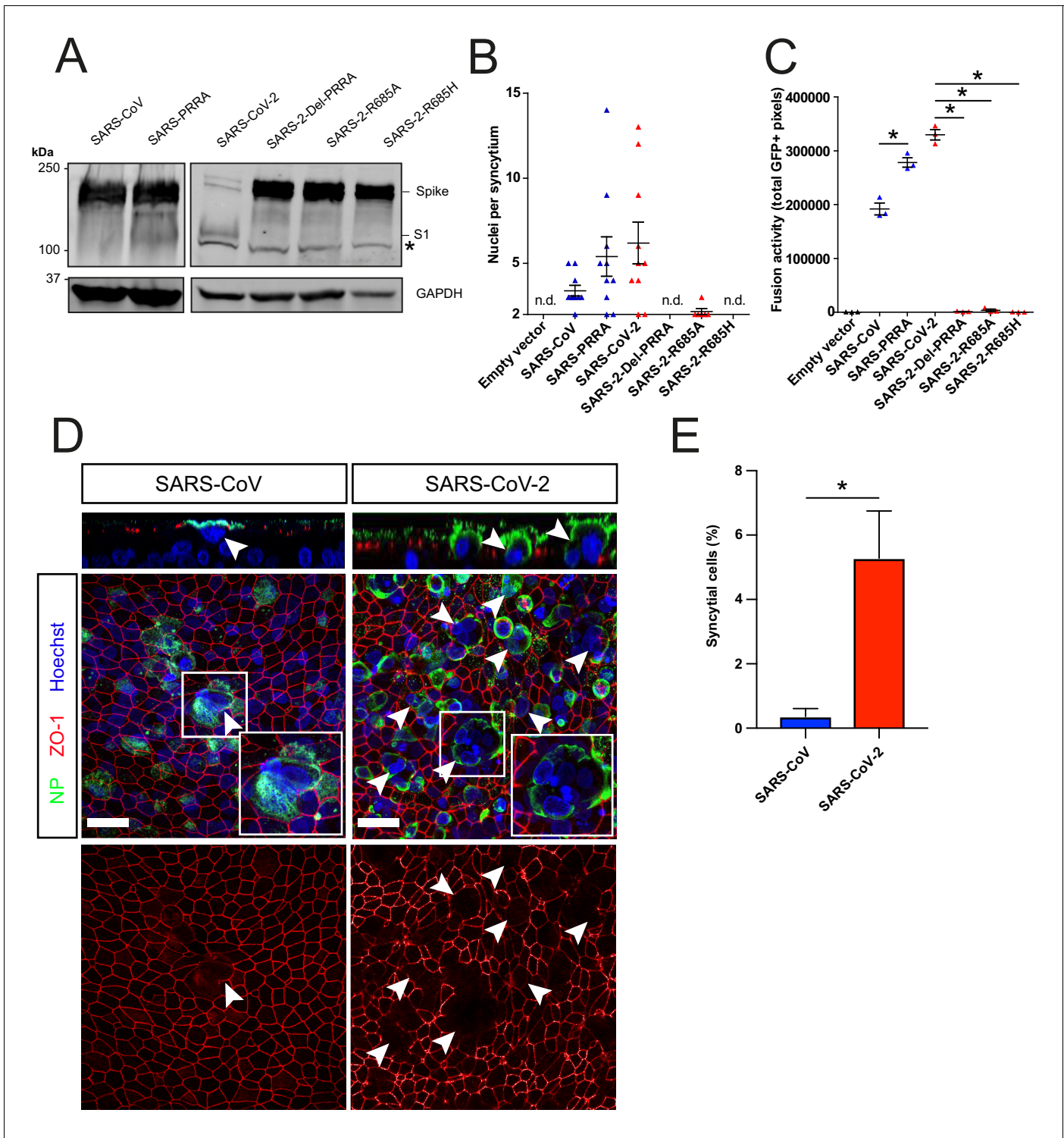


Figure 3. The SARS-CoV-2 multibasic cleavage site facilitates cell–cell fusion and SARS-CoV-2 is more fusogenic than SARS-CoV on human airway organoids. (A) Proteolytic cleavage of SARS-CoV-2 S, SARS-CoV S, and S mutants was assessed by overexpression in HEK-293T cells and subsequent western blots for S1. GAPDH was used as a loading control. Asterisk indicates an unspecific band. (B and C) Fusogenicity of SARS-CoV-2 S, SARS-CoV S, and S mutants was assessed after 18 hr by counting the number of nuclei per syncytium (B) and by measuring the sum of all GFP+ pixels per well (C). Statistical analysis was performed by one-way ANOVA on SARS-CoV or SARS-CoV-2 S-mediated fusion compared with its respective mutants. * $p < 0.05$ (C). (D) Differentiated bronchiolar hAO cultures were infected at an MOI of 1 with SARS-CoV or SARS-CoV-2. Seventy-two hours postinfection they were fixed and stained for nucleoprotein (NP; green) and tight junctions (ZO1; red) to image syncytia. Nuclei were stained with hoechst (blue). Scale bars indicate 20 μm . Arrows indicate syncytial cells. (E) Percentage of syncytial cells of total number of infected cells per field of 0.1 mm^2 . Five fields were

Figure 3 continued on next page

Figure 3 continued

counted. T-test was performed for statistical analysis. * $p < 0.05$. Experiments were performed in triplicate (C). Representative experiments from at least two independent experiments are shown. Error bars indicate SEM. hAO, human airway organoids; H p.i., hours postinfection; MOI, multiplicity of infection; n.d., not detected.

The online version of this article includes the following figure supplement(s) for figure 3:

Figure supplement 1. A GFP complementation based assay for assessing coronavirus fusogenicity.

postinfection, SARS-CoV-2 infection spread in hAOs treated with dimethyl sulfoxide (DMSO) or E64D, but only rare single cells were observed after camostat treatment (**Figure 5B**). Next, we tested whether virus replication was affected by camostat pretreatment of the hAOs. After infection at an MOI of 2, replication was assessed at 2, 24, and 48 hr postinfection by RT-qPCR and live virus titration. In the control hAOs, SARS-CoV-2 replicated to high titers, while camostat reduced replication by approximately 90% (**Figure 5C–E**). We also tested the effect of camostat in 2D differentiated hAOs at air–liquid interface using a low MOI of 0.1. Here, viral titers in apical washes did not increase after camostat pretreatment (**Figure 5F**), whereas replication to moderate titers was observed in the control wells. These findings indicate that SARS-CoV-2 utilizes serine proteases for efficient entry into relevant human airway cells and serine protease inhibition decreases replication.

Discussion

SARS-CoV-2 harbors an MBCS in its S protein. Recent findings show that replacing this site with the SARS-CoV monobasic cleavage site decreases PP infectivity on the adenocarcinoma cell line Calu-3, suggesting that this motif is a human airway adaptation (**Hoffmann et al., 2020a**). This raised the question whether similar findings would be obtained in relevant lung cells. In this study, we found that the SARS-CoV-2 MBCS alters tropism by increasing infectivity on hAOs. Furthermore, we report that the MBCS increases S protein fusogenicity, entry rate, and serine protease usage. Blocking serine proteases, but not cathepsins, in hAOs effectively inhibited SARS-CoV-2 entry and replication, suggesting that serine protease-mediated entry is the main entry route in vivo.

In contrast to SARS-CoV-2, SARS-CoV does not contain an MBCS, yet infects Calu-3 cells with similar efficiency. Introducing an MBCS to SARS-CoV S did not increase infectivity, indicating that the SARS-CoV S has other adaptations to enter airway cells. These data are in agreement with a study that observed no benefit of furin cleavage on SARS-CoV infectivity (**Follis et al., 2006**). Whereas SARS-CoV-2 appears to have adapted to increase fusogenicity and serine protease-mediated S activation for rapid plasma membrane entry, SARS-CoV may have specific adaptations to enter these cells more slowly. Slower viral dissemination may explain why most SARS-CoV patients entered the infectious phase of the disease after symptom onset (**Cheng et al., 2004; Peiris et al., 2003a**). This could have played a role in the 2003 SARS-CoV epidemic, allowing strict public health interventions including quarantining of symptomatic people and contact tracing to halt viral spread. For SARS-CoV-2, however, several studies have reported that individuals can transmit the virus to others before they become symptomatic (**Bai et al., 2020; Huang et al., 2020; Kimball et al., 2020; Wei et al., 2020b; Wiersinga et al., 2020**). Whether differences in entry rate allow SARS-CoV-2 to spread more efficiently in the human airway compared with SARS-CoV remains to be investigated. It will be interesting to assess this using authentic SARS-CoV-2 containing MBCS mutations, which requires a reverse genetic system, not available to this study at present. Whether cell–cell fusion also plays a role in virus dissemination needs to be determined. In a cell–cell fusion assay and in hAOs cultured at air–liquid interface, we show that SARS-CoV-2 is more fusogenic than SARS-CoV and that fusogenicity is increased by the SARS-CoV-2 S MBCS. The role of cell–cell fusion in coronavirus transmission and pathogenesis has not been investigated in detail, but it could be a strategy to avoid extracellular immune surveillance and may increase the viral dissemination rate in the airways in vivo. Whether the MBCS also affects entry into cells of other organs needs to be investigated further. Although SARS-CoV-2 symptoms are mainly respiratory, recent reports indicate frequent extrapulmonary manifestations, including but not limited to thrombotic complications, acute kidney injury, gastrointestinal symptoms, dermatologic complications, and anosmia (**Gupta et al., 2020**). Of note, acute kidney injury was uncommon during the SARS-CoV epidemic (**Chu et al., 2005**). It is

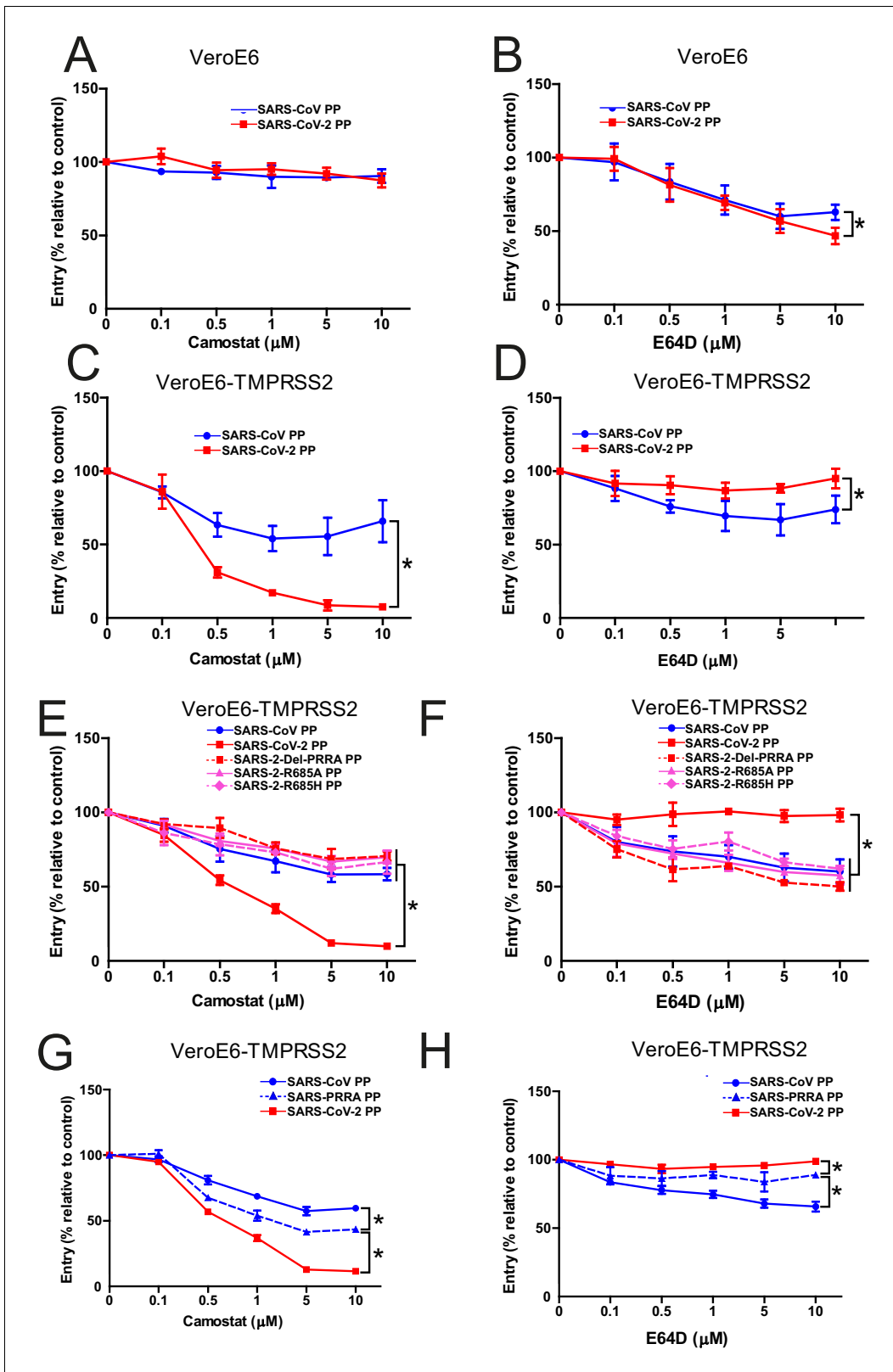


Figure 4. The SARS-CoV-2 multibasic cleavage site increases serine protease usage. (A and B) SARS-CoV PP and SARS-CoV-2 PP entry route on VeroE6 cells pretreated with a concentration range of camostat (A) or E64D (B) to inhibit serine proteases and cathepsins, respectively. (C and D) SARS-CoV PP and SARS-CoV-2 PP entry route on VeroE6-TMPRSS2 cells pretreated with a concentration range of camostat (C) or E64D (D) to inhibit serine proteases and cathepsins, respectively. T-test was performed for statistical analysis at the highest concentration. * $p < 0.05$. (E and F) Entry route of SARS-CoV-2 PP Figure 4 continued on next page

Figure 4 continued

and MBCS mutants on VeroE6-TMPRSS2 cells pretreated with a concentration range of camostat (E) or E64D (F) to inhibit serine proteases and cathepsins, respectively. One-way ANOVA was performed for statistical analysis comparing all groups to SARS-CoV-2 PPs at the highest concentration. * $p < 0.05$. (G and H) Entry route of SARS-CoV PPs and SARS-PRRA PPs on VeroE6-TMPRSS2 cells pretreated with a concentration range of camostat (G) or E64D (H) to inhibit serine proteases and cathepsins, respectively. One-way ANOVA was performed for statistical analysis comparing all groups to SARS-PRRA PPs at the highest concentration. * $p < 0.05$. ANOVA, analysis of variance; MBCS, multibasic cleavage site; PP, pseudoparticles. Representative experiments in triplicate from at least two independent experiments are shown. Error bars indicate SD.

unclear at this moment whether these manifestations are the result of extrapulmonary viral replication.

Using VeroE6-TMPRSS2 cells that have both active serine protease- and cathepsin-mediated entry pathways, we show that the MBCS increases serine protease-mediated S activation, while decreasing cathepsin-mediated S activation. This indicates that the MBCS could be an adaptation to serine protease-mediated entry. Whether this site improves S activation by any protease or by serine proteases specifically remains to be tested. Encountering serine proteases first may result in more plasma membrane entry over endosomal entry. More efficient fusion of multibasic motif containing S proteins may be caused by increased S2' cleavage due to higher accessibility of a S1/S2 cleaved S compared with an uncleaved S. S1/S2 cleavage was recently shown to increase the binding of S to ACE2 (Wrobel et al., 2020). Recent reports indicate that neuropilins (NRP) may be an additional entry factor for SARS-CoV-2 (Cantuti-Castelvetri et al., 2020; Daly et al., 2020). This is an interesting hypothesis as ACE2 expression (mRNA and protein) is relatively low in the lungs, whereas NRP expression appears to be abundant. NRP1 binds peptides with an exposed C-terminal arginine, such as furin-cleaved proteins, and a SARS-CoV-2 mutant with an altered MBCS did not depend on NRP1 for infectivity (Cantuti-Castelvetri et al., 2020). Therefore, it was concluded that NRP1 may promote the interaction of the S1/S2-cleaved virus with ACE2. However, Daly and colleagues observed that NRP1 knockdown did not affect cellular attachment, but did enhance entry and syncytium formation. Therefore, we suggest that NRP1 may facilitate S2' cleavage by exposing this site or S1 dissociation after S2' cleavage for timely exposure of the fusion peptide and subsequent fusion. Structural changes caused by S1/S2 cleavage may affect protease accessibility or protein interactions at the cell membrane as well as increase subsequent S2' cleavage.

While mutations in the SARS-CoV-2 MBCS decreased airway cell infectivity, they increased infectivity on VeroE6 cells. Several groups have reported mutations or deletions in or around the SARS-CoV-2 MBCS that arise in cell culture on VeroE6 cells (Klimstra et al., 2020; Lau et al., 2020; Ogando et al., 2020), indicating that the lack of an MBCS creates a selective advantage in cell culture on VeroE6 cells. The mechanism behind this remains unknown. The increased infectivity of MBCS mutants was not observed by Hoffmann et al., 2020a, but in that study, complete cleavage motifs including four amino acids N-terminally from the minimal RXXR cleavage site were exchanged between SARS-CoV-2 and SARS-CoV (Hoffmann et al., 2020a). In contrast, we mutated single sites or removed/inserted only the PRRA motif. Importantly, a cell culture-adapted virus containing a complete deletion of the MBCS was recently shown to be attenuated in hamsters (Lau et al., 2020). These studies support our findings that the SARS-CoV-2 MBCS affects tropism, facilitates airway cell entry, and show that proper characterization of virus stocks is essential.

Entry inhibition has been proposed as an effective treatment option for SARS-CoV-2. Chloroquine can block SARS-CoV and SARS-CoV-2 entry in vitro into VeroE6 cells (Vincent et al., 2005; Wang et al., 2020), but does not block entry into cells expressing serine proteases (Calu-3 and Vero-TMPRSS2) (Hoffmann et al., 2020c). This is expected, as chloroquine acts in the endosome, while the endosomal entry pathway is not utilized in serine protease expressing cells. As lung cells express serine proteases, inhibitors that block endosomal entry are likely to be ineffective in vivo. These findings highlight that drug screens should be performed directly in relevant cells to prevent wasting resources. Our study shows that SARS-CoV-2 replication in hAOs infected with a high MOI is inhibited ~90% by camostat, suggesting that this drug may be effective in vivo. Future studies assessing the efficacy and safety of camostat in animal models should be conducted. For SARS-CoV, camostat improved survival to 60% in a lethal mouse model (Zhou et al., 2015). In the same study, inhibition of cathepsins using a cysteine protease inhibitor was ineffective, supporting a critical role for serine proteases in viral spread and pathogenesis in vivo. In Japan, camostat has been clinically

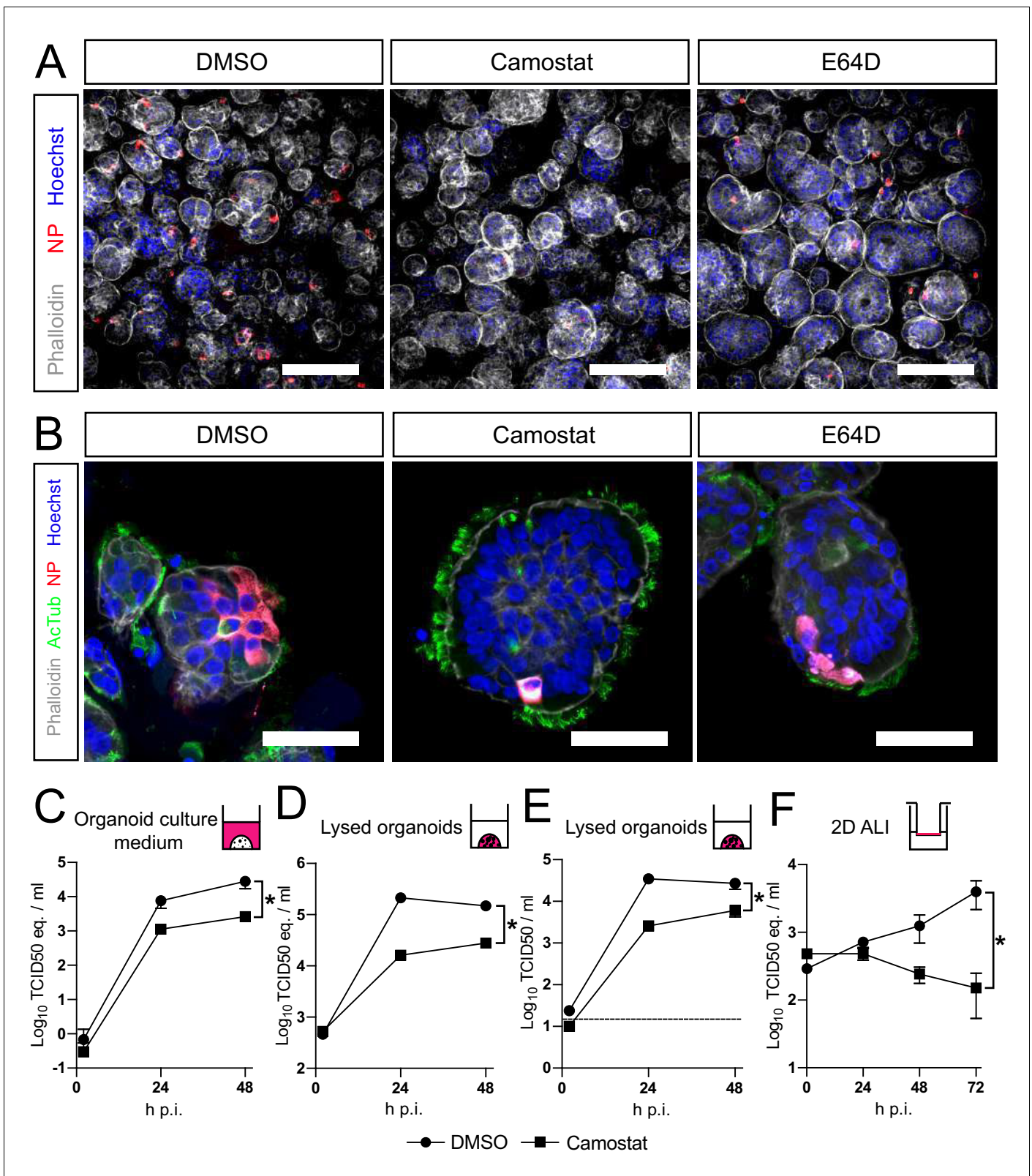


Figure 5. SARS-CoV-2 entry and replication are dependent on serine proteases in human airway organoids. (A and B) Differentiated bronchiolar (A) or bronchial (B) hAO cultures were infected at an MOI of 2. Sixteen hours (A) or 24 hr (B) postinfection they were fixed and stained for viral nucleoprotein (red). Nuclei were stained with hoechst (blue) and actin was stained using phalloidin (white). AcTub stains ciliated cells (green). Scale bars indicate 200 μ m in (A) and 50 μ m in (B). Representative images are shown from two independent experiments. (C–E) Replication kinetics of SARS-CoV-2 in

Figure 5 continued on next page

Figure 5 continued

bronchiolar hAO cultures pretreated with camostat or carrier (DMSO). (C and D) TCID50 equivalents (eq.) per mL are shown in culture medium (C) and lysed organoids (D). Circles indicate DMSO-treated organoids, whereas squares indicate camostat-treated organoids. (E) Live virus titers (TCID50/mL) in lysed organoids. Dotted line indicates limit of detection. (F) Replication kinetics of SARS-CoV-2 in 2D tracheal air-liquid interface airway cultures pretreated with camostat or carrier (DMSO). TCID50 eq./mL in apical washes are shown. Two-way ANOVA was performed for statistical analysis. Error bars indicate SEM. * $p < 0.05$. DMSO, dimethyl sulfoxide; hAO, human airway organoid; H p.i., hours postinfection; MOI, multiplicity of infection.

approved to treat chronic pancreatitis and thus represents a potential therapy for respiratory coronavirus infections.

We demonstrate that SARS-CoV-2 enters hAOs using serine proteases, but not using cathepsins, clarifying existing discrepancies between human cell lines and suggesting that serine-protease-mediated entry is the main entry route in vivo. In addition, our findings indicate that the multibasic cleavage motif in the SARS-CoV-2 S protein is an adaptation to this viral entry strategy, and can guide the design of entry inhibitors to combat COVID-19.

Materials and methods

Key resources table

Reagent type (species) or resource	Designation	Source or reference	Identifiers	Additional information
VeroE6 cells (<i>Cercopithecus aethiops</i>)	Monkey kidney cell line	ATCC	CRL 1586TM	
Vero cells (<i>Cercopithecus aethiops</i>)	Monkey kidney cell line	WHO	RCB 10-87	
Calu-3 (<i>Homo sapiens</i>)	Lung adenocarcinoma cell line	ATCC	HTB 55	
SARS-CoV-2 BavPat1	SARS-CoV-2	Dr. Christian Drosten	European Virus Archive Global #026V-03883	
SARS-CoV HKU39849	SARS-CoV	Dr. Malik Peiris	N/A	
Airway tissue for organoids (<i>Homo sapiens</i>)	Airway organoids	This study	This study	
Aloxistatin	E64D	MedChemExpress	Cat# HY-100229	
Camostat mesylate	Camostat	Sigma	Cat# SML0057	
Hexadimethrine bromide	Polybrene	Sigma	107689-10G	
Polyethylenimine linear	Polyethylenimine	Polysciences	Cat# 23966	
Hygromycin B	Hygromycin B	Invitrogen	Cat# 10843555001	
G418, Geneticin	Geneticin	Invitrogen	Cat# 10131035	
Opti-MEM I (1×) + GlutaMAX	Opti-MEM I (1×) + GlutaMAX	Gibco	Cat# 51985-042	
Advanced DMEM/F12	Advanced DMEM/F12	Thermo Fisher scientific	Cat# 12634-010	
AO medium	AO medium	Sachs et al., 2019	N/A	
Pneumacult ALI medium	Pneumacult ALI medium	Stemcell	Cat # 05001	

Continued on next page

Continued

Reagent type (species) or resource	Designation	Source or reference	Identifiers	Additional information
TrypLE	TrypLE	Thermo Fisher Scientific	Cat# 12605010	
Cultrex Basement Membrane Extract, Type 2	Basement membrane extract	R&D Systems	Cat# 3533-005-02	
12 mm Transwell with 0.4 µm Pore Polyester Membrane Insert, Sterile	Transwell inserts	Corning	Cat# 3460	
Collagen Type I, High concentration Rat tail	Collagen	Corning	Cat# 354249	
0.45 µm low protein binding filter	0.45 µm low protein binding filter	Millipore	Cat# SLHV033RS	
Recombinant DNA reagent	pCMV-S (CUHK-W1)	Sino Biological	Cat# VG40150-G-N	Encoding S of isolate CUHK-W1;
Recombinant DNA reagent	pCAGGS-S (CUHK-W1)	This study	This study	Encoding S of isolate CUHK-W1;
Recombinant DNA reagent	pCAGGS-S (Wuhan-Hu-1)	This study	This study	Encoding S of isolate Wuhan-Hu-1
Recombinant DNA reagent	pQXCIN	Clontech	Cat# 631516	Retro-X Q vector set
Recombinant DNA reagent	pQXCIH	Clontech	Cat# 631516	Retro-X Q vector set
Recombinant DNA reagent	pQXCIP-GFP1-10	Addgene	Cat# 68715	GFP1-10
Recombinant DNA reagent	pCDNA-TMPRSS2-FLAG	Genscript	OHu13675D	Human TMPRSS2 cDNA
Recombinant DNA reagent	pCAGGS-β-Actin-7xGFP11-P2A-BFP	This study	This study	β-Actin-7xGFP11-P2A-BFP
Recombinant DNA reagent	pBS-gag-pol	Addgene	Cat# 35614	gag-pol
Recombinant DNA reagent	pMD2.G	Addgene	Cat# 12259	VSV-G
Recombinant DNA reagent	pVSV-eGFP-dG	Addgene	Cat# 31842	VSV delta G genomic plasmid
Recombinant DNA reagent	pCAG-VSV-P	Addgene	Cat# 64088	P protein
Recombinant DNA reagent	pCAG-VSV-L	Addgene	Cat# 64085	L protein
Recombinant DNA reagent	pCAG-VSV-N	Addgene	Cat# 64087	N protein
Recombinant DNA reagent	pCAGGS-T7Opt	Addgene	Cat# 65974	T7 polymerase
Antibody	Mouse-anti-SARS-CoV NP (monoclonal)	Sino Biological	Cat# 40143-MM05	IF (1:400)
Antibody	Rabbit-anti-SARS-CoV NP (polyclonal)	Sino Biological	Cat# 40143-T62	IF (1:400)

Continued on next page

Continued

Reagent type (species) or resource	Designation	Source or reference	Identifiers	Additional information
Antibody	Goat anti-ACE2 (polyclonal)	R&D Systems	Cat# AF933	IF (1:200)
Antibody	Mouse anti-TMPRSS2 (monoclonal)	Santa Cruz	Cat# sc-515727	IF (1:200)
Antibody	Rabbit-anti-goat	Dako	Cat# P0160	IF (1:400)
Antibody	Goat-anti-mouse	Dako	Cat# P0260	IF (1:400)
Antibody	Mouse anti-VSV (monoclonal)	Absolute Antibody	Cat# EB0010	Pseudoparticle production (1:50,000)
Antibody	Goat anti-rabbit IgG (H+L) Alexa Fluor Plus 488	Invitrogen	Cat# A32731	IF (1:400)
Antibody	Goat anti-mouse IgG (H+L) Alexa Fluor Plus 488	Invitrogen	Cat# A11029	IF (1:400)
Antibody	Goat anti-mouse IgG (H+L) Alexa Fluor Plus 594	Invitrogen	Cat# A21125	IF (1:400)
Antibody	Mouse anti-double stranded RNA IgG2A (monoclonal)	Scicons	J2 clone	IF (1:500)
Antibody	Mouse-anti-ZO1 IgG1 (monoclonal)	Invitrogen	Cat# 33-9100	IF (1:200)
Antibody	Mouse-anti-CC10 IgG1 Alexa Fluor 594 (monoclonal)	Santa Cruz Biotechnology	Cat# sc-390313 AF594	IF (1:100)
Antibody	Mouse-anti-AcTub IgG2A Alexa Fluor 488 (monoclonal)	Santa Cruz Biotechnology	Cat# sc-23950 AF488	IF (1:100)
Antibody	Mouse anti-MUC5AC (monoclonal)	Invitrogen	Cat# MA5-12178	IF (1:100)
Antibody	Mouse-anti-FOXJ1 IgG1 (monoclonal)	eBioscience	Cat# 14-9965-82	IF (1:200)
Antibody	Rabbit anti-SARS-CoV S1 (polyclonal)	Sino Biological	Cat# 40150-T62	WB (1:1000)
Antibody	Mouse anti-GAPDH (monoclonal)	Santa Cruz Biotechnology	Cat# sc-32233	WB (1:1000)
Pierce Silver Stain for Mass Spectrometry	Silver stain	Pierce	Cat# 24600	
TO-PRO-3 Iodide	TO-PRO3	ThermoFisher	Cat# T3605	
Phalloidin CruzFluor 647 Conjugate	Phalloidin	Santa Cruz	Cat# ec-363796	
Hoechst 33342, Trihydrochloride, Trihydrate	Hoechst	ThermoFisher	Cat# H1399	

Continued on next page

Continued

Reagent type (species) or resource	Designation	Source or reference	Identifiers	Additional information
4× Laemmli Sample Buffer	Laemmli	Bio-Rad	Cat# 1610747	
Odyssey CLx	Odyssey CLx	Licor		
Amersham Typhoon Biomolecular Imager	Amersham Typhoon Biomolecular Imager	GE Healthcare		
Amersham Imager 600	Amersham Imager 600	GE Healthcare		
LSM700 confocal microscope	LSM700 confocal microscope	Zeiss		
Carl ZEISS Vert.A1	Carl ZEISS Vert.A1	Zeiss		
ZEN software	ZEN	Zeiss		
ImageQuant TL 8.2	ImageQuant TL 8.2	GE Healthcare		
Studio Lite Ver 5.2	Studio Lite Ver 5.2	Licor		
GraphPad PRISM 8	GraphPad PRISM 8	GraphPad		
Adobe Illustrator	Illustrator	Adobe Inc		

Viruses and cells

Vero, VeroE6, and VeroE6 stable cell lines were maintained in Dulbecco's modified Eagle's medium (DMEM, Gibco) supplemented with 10% fetal calf serum (FCS), HEPES (20 mM, Lonza), sodium bicarbonate (0.075%, Gibco), penicillin (100 IU/mL), and streptomycin (100 IU/mL) at 37°C in a humidified CO₂ incubator. Calu-3 and Calu-3-stable cell lines were maintained in Eagle's minimal essential medium (ATCC) supplemented with 20% FCS, penicillin (100 IU/mL), and streptomycin (100 IU/mL) at 37°C in a humidified CO₂ incubator. HEK-293T cells were cultured in DMEM supplemented with 10% FCS, sodium pyruvate (1 mM, Gibco), non-essential amino acids (1×, Lonza), penicillin (100 IU/mL), and streptomycin (100 IU/mL) at 37°C in a humidified CO₂ incubator. TMPRSS2 and GFP1-10 overexpression cells were maintained in medium containing hygromycin (Invitrogen) and geneticin (Invitrogen), respectively. SARS-CoV-2 (isolate BetaCoV/Munich/BavPat1/2020; European Virus Archive Global #026 V-03883; kindly provided by Dr. C. Drosten) and SARS-CoV (isolate HKU39849) were propagated on Vero cells in Opti-MEM I (1×) + GlutaMAX (Gibco), supplemented with penicillin (100 IU/mL) and streptomycin (100 IU/mL) at 37°C in a humidified CO₂ incubator. Vero, VeroE6, and Calu-3 cells were purchased from ATCC. Cultures were routinely tested for mycoplasma. The SARS-CoV-2 isolate was obtained from a clinical case in Germany, diagnosed after returning from China. Stocks were produced by infecting cells at an MOI of 0.01 and incubating the cells for 72 hr. The culture supernatant was cleared by centrifugation and stored in aliquots at −80°C. Stock titers were determined by preparing 10-fold serial dilutions in Opti-MEM I (1×) + GlutaMAX. Aliquots of each dilution were added to monolayers of 2 × 10⁴ VeroE6 cells in the same medium in a 96-well plate. Plates were incubated at 37°C 5% CO₂ for 5 days and then examined for cytopathic effect. The TCID₅₀ was calculated according to the method of Spearman and Kärber. All work with infectious SARS-CoV and SARS-CoV-2 was performed in a Class II Biosafety Cabinet under BSL-3 conditions at Erasmus Medical Center.

Cloning

Codon-optimized SARS-CoV (isolate CUHK-W1; VG40150-G-N) S expression plasmids (pCMV) were ordered from Sino-Biological and subcloned into pCAGGS using the Clal and KpnI sites. The last 19

amino acids containing the Golgi retention signal of the SARS-CoV S protein were deleted to enhance PP production. Codon-optimized cDNA encoding SARS-CoV-2 S glycoprotein (isolate Wuhan-Hu-1) with a C-terminal 19 amino acid deletion was synthesized and cloned into pCAGGS in between the EcoRI and BglII sites. S expressing pCAGGS vectors were used for GFP complementation fusion assays, and equivalent S proteins with the C-terminal deletion were used for the production of PPs, as described in Material and methods. The cDNA encoding GFP1-10 was obtained from Addgene and was subcloned into pQXCIN (Clontech) in between BamHI and EcoRI to obtain the pQXCIN-GFP1-10 vector. The cDNA encoding human TMPRSS2 (NM_005656; OHu13675D) was obtained from Genscript. The cDNA fused to a C-terminal HA tag was subcloned into pQXCIH (Clontech) in between the NotI and PacI sites to obtain the pQXCIH-TMPRSS2-HA vector. A synthetic DNA construct of β -actin-7xGFP11-P2A-BFP was ordered from GenScript and subcloned into pGAGGS using EcoRI and BglII. SARS-CoV and SARS-CoV-2 S protein mutations (SARS-PRRA, SARS-2-Del-PRRA, SARS-2-R685A, SARS-2-R685H) were generated by subcloning synthetic DNA constructs (Genscript) containing the desired mutations into the pCAGGS-S vectors or by mutagenesis PCR.

Isolation, culture, and differentiation of human airway stem cells

Adult lung tissue was obtained from residual, tumor-free material obtained at lung resection surgery for lung cancer. The Medical Ethical Committee of the Erasmus MC Rotterdam granted permission for this study (METC 2012–512). Isolation, culture, and differentiation were performed as described previously (Lamers *et al.*, 2020) according to a protocol adapted from Sachs *et al.*, 2019. Differentiation time on air–liquid interphase was 10–11 weeks. For this study, we used carefully dissected out bronchial material for the generation of human bronchial airway organoids. Bronchiolar organoids were generated from distal lung parenchymal material. Tracheal stem cells were collected from tracheal aspirates of intubated preterm infants (<28 weeks gestational age) (Hiemstra *et al.*, 2020) and cultured as described before (Sachs *et al.*, 2019). For the tracheal aspirates, informed consent was obtained from parents, and approval was given by the Medical Ethical Committee (METC no. MEC-2017–302). All donor materials were completely anonymized.

Authentic virus infection of primary airway cells

To assess differences in syncytium formation, 2D air–liquid interface differentiated airway cultures were washed three times with 500 μ L advanced DMEM/F12 (AdDF+++; Gibco) before inoculation from the apical side at an MOI of 1 in 200 μ L AdDF+++ per well. Next, cultures were incubated at 37°C 5% CO₂ for 2 hr before washing four times in 500 μ L AdDF++. Cultures were washed daily from the apical side with 300 μ L AdDF+++ to facilitate virus spread. At 72 hr postinfection, cells were fixed for immunofluorescent staining.

To determine the effect of camostat on SARS-CoV-2 entry, we incubated bronchial or bronchiolar cultures that were differentiated at air–liquid interface for 10–11 weeks with 100% dispase in the basal compartment of a 12 mm Transwell insert. After a 10 min incubation step at 37°C 5% CO₂, dispase was removed and cold 500 μ L AdDF+++ was pipetted onto the apical side of the Transwell to dislodge the pseudostratified epithelial layer, which was subsequently mechanically sheared by pipetting using a P1000 tip. The resulting epithelial fragments were washed twice in 5 mL AdDF+++ before treatment with 10 μ M camostat, 10 μ M E64D, or carrier (DMSO) in Pneumacult (PC) ALI medium (Stemcell) on ice for 1 hr. Next, fragments were infected at an MOI of 2 for 2 hr at 37°C 5% CO₂ in the presence of inhibitors or DMSO. Subsequently, fragments were washed three times in 5 mL cold AdDF+++ before being embedded in 30 μ L BME (Type 2; R and D Systems) per well in a 48-well plate. Approximately 200,000 cells were plated per well. After solidification of the BME, 200 μ L PC was added per well and plates were incubated at 37°C 5% CO₂.

To assess SARS-CoV-2 replication in the presence of camostat, bronchiolar airway organoids, or 2D air–liquid interface differentiated tracheal airway cultures were infected as described above. For organoids, culture medium was collected at the indicated time points and frozen at –80°C. After culture medium collection, BME droplets containing organoids were resuspended in 200 μ L AdDF+++ and samples were frozen at –80°C to lyse the cells. To assess 2D air–liquid interface differentiated airway culture replication kinetics, apical washes were collected at the indicated time points by adding 200 μ L AdDF+++ apically, incubating for 15 min at 37°C 5% CO₂, and collecting the sample

before storage at -80°C . For virus titrations using RT-qPCR (Lamers *et al.*, 2020) or TCID50 determination, samples were thawed and centrifuged at $500 \times g$ for 3 min. For TCID50 determination, six replicates were performed per sample.

Fixed immunofluorescence microscopy and immunohistochemistry

Transwell inserts were fixed in formalin, permeabilized in 70% ethanol, and blocked for 60 min in 10% normal goat serum or 3% bovine serum albumin in phosphate-buffered saline (PBS) (blocking buffer). For organoids, 0.1% triton X-100 was added to the blocking buffer to increase antibody penetration. Cells were incubated with primary antibodies overnight at 4°C in blocking buffer, washed twice with PBS, incubated with corresponding secondary antibodies Alexa488- and 594-conjugated secondary antibodies (1:400; Invitrogen) in blocking buffer for 2 hr at room temperature, washed two times with PBS, incubated with indicated additional stains (TO-PRO3, phalloidin-633 [SC-363796, Santa Cruz Biotechnology], Hoechst), washed twice with PBS, and mounted in Prolong Antifade (Invitrogen) mounting medium.

SARS-CoV-2 and SARS-CoV were stained with mouse-anti-SARS-CoV nucleoprotein (40143-MM05, 1:400, Sino Biological) or rabbit-anti-SARS-CoV nucleoprotein (40143-T62, 1:400, Sino Biological). Tight junctions were stained using mouse-anti-ZO1 (ZO1-1A12, 1:200, Invitrogen). Club cells and goblet cells were stained with mouse-anti-CC10 (sc-390313 AF594, 1:100, Santa Cruz Biotechnology) and mouse anti-MUC5AC (MA5-12178, 1:100, Invitrogen), respectively. Ciliated cells were stained with mouse-anti-FOXJ1 (14-9965-82, 1:200, eBioscience) and mouse-anti-AcTub (sc-23950 AF488, 1:100, Santa Cruz Biotechnology). For lineage marker stainings, formalin-fixed inserts were paraffin-embedded, sectioned, and deparaffinized as described before prior to staining (Rockx *et al.*, 2020). Samples were imaged on an LSM700 confocal microscope using ZEN software (Zeiss). Representative images were acquired and shown as Z-projections, single slices, or XZ cross sections.

Immunohistochemistry was performed as described previously (Rockx *et al.*, 2020) on formalin-fixed, paraffin-embedded Transwell inserts. ACE2 and TMPRSS2 were stained using goat-anti-hACE2 (AF933, 1:200, R and D Systems) and mouse-anti-TMPRSS2 (sc-515727, 1:200, Santa Cruz Biotechnology) and visualized with rabbit-anti-goat (P0160, 1:200, Dako) and goat-anti-mouse (P0260, 1:100, Dako) horseradish peroxidase-labeled secondary antibody, respectively. Samples were counterstained using hematoxylin.

Generation of stable cell lines expressing GFP1-10 and TMPRSS2

VeroE6 GFP1-10, VeroE6-TMPRSS2 cells, VeroE6-TMPRSS2 GFP1-10 cells, and Calu-3 GFP1-10 cells were generated by retroviral transduction. To produce the retrovirus, $10 \mu\text{g}$ pQXCIH-TMPRSS2-HA or pQXCIN-GFP1-10 was co-transfected with polyethylenimine (PEI) with $6.5 \mu\text{g}$ pBS-gag-pol (Addgene #35614) and $5 \mu\text{g}$ pMD2.G (Addgene #12259) in a 10 cm dish of 70% confluent HEK-293T cells in Opti-MEM I ($1\times$) + GlutaMAX. Retroviral particles were harvested at 72 hr post-transfection, cleared by centrifugation at $2000 \times g$, filtered through a $0.45 \mu\text{m}$ low protein binding filter (Millipore), and used to transduce designated cells. Polybrene (Sigma) was added at a concentration of $4 \mu\text{g}/\text{mL}$ to enhance transduction efficiency. Transduced cells were selected with hygromycin B (Invitrogen) for TMPRSS2 cells and/or geneticin (Invitrogen) for GFP1-10 cells.

GFP complementation fusion assay

HEK-293T cells were grown in six-well format to 70–80% confluency and were transfected with $1.5 \mu\text{g}$ pGAGGS-spike (all coronavirus S variants described above) DNA and pGAGGS- β -Actin-P2A-7xGFP11-BFP DNA or empty vector DNA with PEI in a ratio of 1:3 (DNA:PEI). Beta-actin was tagged with 7xGFP11 expressed in tandem and blue fluorescent protein (BFP). The two genes were separated by a P2A self-cleaving peptide. Two variants of this construct were used. One variant contained a GSG linker located N-terminally from the P2A site to improve self-cleavage and this construct was used in qualitative confocal microscopy experiments. A variant lacking the GSG linker was less efficiently cleaved as indicated by both cytoplasmic and nuclear localized GFP, but this generated an equal distribution of GFP throughout the cell and therefore it was used for all fusion assays in which the sum of all GFP+ pixels was calculated. Transfected HEK-293T cells were incubated overnight at 37°C 5% CO_2 . GFP1-10 expressing cells were seeded in a 12-well plate to achieve 90–100%

confluency after overnight incubation at 37°C 5% CO₂ and medium was refreshed with Opti-MEM I (1×) + GlutaMAX. HEK-293T cells were resuspended in PBS by pipetting to generate a single-cell suspension and added to GFP1-10 expressing cells in a ratio of 1:80 (HEK-293T cells: GFP1-10 expressing cells). Fusion events were quantified by detecting GFP+ pixels after 18 hr incubation at 37°C 5% CO₂ using Amersham Typhoon Biomolecular Imager (channel Cy2; resolution 10 μm; GE Healthcare). Data was analyzed using the ImageQuant TL 8.2 image analysis software (GE Healthcare) by calculating the sum of all GFP+ pixels per well. For nuclear counting fluorescence microscopy images were obtained with a Carl ZEISS Vert.A1 microscope paired with an AxioCam ICm1 camera and Colibri seven laser (469/38 nm for GFP and 365/10 nm for BFP) using ZEN analysis software (20× magnification). Nuclei per syncytia were calculated by counting BFP-positive nuclei after 18 hr incubation at 37°C 5% CO₂. Confocal microscopy images were taken on an LSM700 confocal microscope using ZEN software. Representative images were acquired and shown as single slices.

VSV delta G rescue

The protocol for VSV-G PP rescue was adapted from *Whelan et al., 1995*. VSV rescue plasmids pVSV-eGFP-dG (#31842), pMD2.G (#12259), pCAG-VSV-P (#64088), pCAG-VSV-L (#64085), pCAG-VSV-N (#64087), and pCAGGS-T7Opt (#65974) were ordered from Addgene. Briefly, a 70% confluent 10 cm dish of HEK-293T cells was transfected with 10 μg pVSV-eGFP-dG, 2 μg pCAG-VSV-N (nucleocapsid), 2 μg pCAG-VSV-L (polymerase), 2 μg pMD2.G (glycoprotein, VSV-G), 2 μg pCAG-VSV-P (phosphoprotein), and 2 μg pCAGGS-T7Opt (T7 RNA polymerase) using PEI at a ratio of 1:3 (DNA:PEI) in Opti-MEM I (1×) + GlutaMAX. Forty-eight hours post-transfection, the supernatant was transferred onto new plates transfected 24 hr prior with VSV-G. After a further 48 hr, these plates were re-transfected with VSV-G. After 24 hr the resulting PPs were collected, cleared by centrifugation at 2000 × g for 5 min, and stored at −80°C. Subsequent VSV-G PP batches were produced by infecting VSV-G transfected HEK-293T cells with VSV-G PPs at an MOI of 0.1. Titers were determined by preparing 10-fold serial dilutions in Opti-MEM I (1×) + GlutaMAX. Aliquots of each dilution were added to monolayers of 2 × 10⁴ Vero cells in the same medium in a 96-well plate. Three replicates were performed per PP stock. Plates were incubated at 37°C overnight and then scanned using an Amersham Typhoon scanner. Individual infected cells were quantified using ImageQuant TL software. All PP work was performed in a Class II Biosafety Cabinet under BSL-2 conditions at Erasmus Medical Center.

Coronavirus S pseudotyped particle production

For the production of SARS-CoV and SARS-CoV-2 S PPs, as well as MBCS mutant PPs, HEK-293T cells were transfected with 15 μg S expression plasmids. Twenty-four hours post-transfection, the medium was replaced for Opti-MEM I (1×) + GlutaMAX, and cells were infected at an MOI of 1 with VSV-G PPs. Two hours postinfection, cells were washed three times with Opti-MEM I (1×) + GlutaMAX and replaced with medium containing anti-VSV-G neutralizing antibody (clone 8G5F11; Absolute Antibody) at a dilution of 1:50,000 to block remaining VSV-G PPs. The supernatant was collected after 24 hr, cleared by centrifugation at 2000 × g for 5 min, and stored at 4°C until use within 7 days. Coronavirus S PPs were titrated on VeroE6 cells as described above.

Entry route assay

VeroE6, Calu-3, and VeroE6-TMPRSS2 cells were seeded in 24-well plates and kept at 37°C 5% CO₂ overnight to achieve 80–100% confluency by the next day. Cells were pretreated with a concentration range of camostat, E64D, or DMSO (with all conditions containing equal concentrations of DMSO) in Opti-MEM I (1×) + GlutaMAX for 2 hr before infecting with on average 1000 PPs per well. Plates were incubated overnight at 37°C 5% CO₂ before scanning for GFP signal as described above.

Entry speed assay

Calu-3 cells were seeded as for entry route assays and pretreated with 10 μM E64D. After 1 hr, PPs were added per well to achieve 1000 infected cells in the control well. At the same time as addition of PPs, 10 μM camostat was added into the first set of wells (t = 0). DMSO was added to controls.

The same inhibitor was added in the next sets of wells in triplicate 2, 4, and 6 hr postinfection. Plates were incubated overnight at 37°C 5% CO₂ before scanning for GFP signal as described above.

Authentic virus entry speed was performed in the same manner, by infecting Calu-3 cells with 1×10^4 TCID50 SARS-CoV-2 and 5×10^4 TCID50 SARS-CoV. After 12 hr, plates were fixed and blocked as above for transwell inserts. Cells were incubated with mouse-anti-double stranded RNA (Clone J2, 1:500, Scicons) in blocking buffer for 2 hr at room temperature or overnight at 4°C. Cells were washed twice with PBS and stained with Alexa488 conjugated secondary antibody (1:500, Invitrogen) in blocking buffer for an hour at room temperature. Finally, cells were washed twice with PBS and scanned in PBS on the Amersham Typhoon as described above.

Coronavirus S pseudotyped particle concentration

PPs were concentrated on a 10% sucrose cushion (10% sucrose, 15 mM Tris-HCl, 100 mM NaCl, 0.5 mM EDTA) at $20,000 \times g$ for 1.5 hr at 4°C. Supernatant was decanted, and pellet was resuspended overnight at 4°C in Opti-MEM I (1 \times) + GlutaMAX to achieve 100-fold concentration. PPs were titrated and aliquots were lysed in 1 \times Laemmli buffer (Bio-Rad) containing 5% 2-mercaptoethanol for western blot analysis.

PP infection of primary airway cells

To determine the effect of MBCS mutations on SARS-CoV-2 entry, we obtained airway culture fragments from 2D differentiated bronchiolar cultures as described above. Next, fragments were infected with 40 μ L of concentrated wild-type and MBCS mutant PPs for 2 hr at 37°C 5% CO₂. Subsequently, the supernatant was replaced with 30 μ L BME and plated in a 48-well plate. Approximately 200,000 cells were plated per well. After solidification of the BME, 200 μ L PC was added per well and plates were incubated at 37°C 5% CO₂. After overnight incubation, the amount of infected cells and organoids per five fields were counted and images taken using a Carl ZEISS Vert.A1 microscope paired with an AxioCam ICm1 camera and Colibri seven laser (469/38 nm for GFP) using ZEN analysis software.

Spike protein western blot

Concentrated PPs diluted in 4 \times Laemmli loading buffer were boiled for 30 min at 95°C. S transfected HEK-293T cells were lysed using IP Lysis Buffer (Pierce). Cell lysate was rotated for 30 min and centrifuged for 10 min at $15,000 \times g$. Supernatant was used for subsequent protein expression analysis. Lysates were diluted in 4 \times Laemmli loading buffer containing 20% 2-mercaptoethanol and boiled for 30 min at 95°C. PPs and cell lysates were used for sodium dodecyl sulfate (SDS)-polyacrylamide gel electrophoresis analysis using precast 10% TGX gels (Bio-Rad). Gels were run in Tris-glycine-SDS buffer at 50 V for 30 min and subsequently at 120 V for 90 min. Transfer was performed at 300 mA for 55 min onto 0.45 μ m Immobilon-FL PVDF membranes in Tris-glycine buffer containing 20% methanol. Spike was stained using polyclonal rabbit-anti-SARS-CoV S1 (1:1000, Sino Biological) followed by infrared-labeled secondary antibodies (1:20,000, Licor). All cell lysate western blots are stained for GAPDH using a monoclonal mouse-anti-GAPDH antibody (sc-32233, 1:1000, Santa Cruz Biotechnology) followed by infrared-labeled secondary antibodies. Western blots were scanned on an Odyssey CLx and analyzed using Image Studio Lite Ver 5.2 software.

Silver staining

All PP western blots had corresponding silver stains performed to assess the quality of the PP preps and for the detection of VSV-N. Samples boiled in Laemmli buffer for western blot analysis were also ran on a 10% w/v gel at 50 V for 30 min followed by 120 V for 90 min before transferring gel into ultrapure water. Silver stains were performed per manufacturer's instructions using the Silver Stain for Mass Spectrometry Kit (Pierce). Colorimetric images were taken on the Amersham AI600 (GE Healthcare).

Statistical analysis

Statistical analysis was performed with the GraphPad Prism 5 and 8 software using a t-test, one-way ANOVA, or two-way ANOVA followed by a Bonferroni multiple-comparison test.

Acknowledgements

This work was supported by NWO Grant 022.005.032, partly financed by the Netherlands Organization for Health Research and Development (ZONMW) grant agreement 10150062010008 to BLH and co-funded by the PPP Allowance (grant agreement LSHM19136) made available by Health Holland, Top Sector Life Sciences and Health, to stimulate public-private partnerships. The present manuscript was part of the research program of the Netherlands Centre for One Health.

Additional information

Funding

Funder	Grant reference number	Author
Nederlandse Organisatie voor Wetenschappelijk Onderzoek	0.22.005.032	Bart L Haagmans
ZonMw	10150062010008	Bart L Haagmans
Health Holland	LSHM19136	Bart L Haagmans

The funders had no role in study design, data collection and interpretation, or the decision to submit the work for publication.

Author contributions

Anna Z Mykytyn, Tim I Breugem, Conceptualization, Formal analysis, Validation, Investigation, Visualization, Methodology, Writing - original draft, Writing - review and editing; Samra Riesebosch, Formal analysis, Investigation, Visualization, Writing - review and editing; Debby Schipper, Petra B van den Doel, Investigation, Writing - review and editing; Robbert J Rottier, Resources, Writing - review and editing; Mart M Lamers, Conceptualization, Formal analysis, Supervision, Validation, Investigation, Visualization, Methodology, Writing - original draft, Writing - review and editing; Bart L Haagmans, Conceptualization, Supervision, Funding acquisition, Writing - review and editing

Author ORCIDs

Anna Z Mykytyn  <https://orcid.org/0000-0001-7188-6871>
Tim I Breugem  <https://orcid.org/0000-0002-5558-7043>
Robbert J Rottier  <http://orcid.org/0000-0002-9291-4971>
Mart M Lamers  <https://orcid.org/0000-0002-1431-4022>
Bart L Haagmans  <https://orcid.org/0000-0001-6221-2015>

Decision letter and Author response

Decision letter <https://doi.org/10.7554/eLife.64508.sa1>
Author response <https://doi.org/10.7554/eLife.64508.sa2>

Additional files

Supplementary files

- Transparent reporting form

Data availability

All data generated or analysed during this study are included in the manuscript and supporting files.

References

- Bai Y, Yao L, Wei T, Tian F, Jin DY, Chen L, Wang M. 2020. Presumed asymptomatic carrier transmission of COVID-19. *Jama* **323**:1406. DOI: <https://doi.org/10.1001/jama.2020.2565>, PMID: 32083643
- Belouzard S, Millet JK, Licitra BN, Whittaker GR. 2012. Mechanisms of coronavirus cell entry mediated by the viral spike protein. *Viruses* **4**:1011–1033. DOI: <https://doi.org/10.3390/v4061011>, PMID: 22816037

- Cantuti-Castelvetri L**, Ojha R, Pedro LD, Djannatian M, Franz J, Kuivanen S, van der Meer F, Kallio K, Kaya T, Anastasina M, Smura T, Levanov L, Szivovica L, Tobi A, Kallio-Kokko H, Österlund P, Joensuu M, Meunier FA, Butcher SJ, Winkler MS, et al. 2020. Neuropilin-1 facilitates SARS-CoV-2 cell entry and infectivity. *Science* **370**: 856–860. DOI: <https://doi.org/10.1126/science.abd2985>, PMID: 33082293
- Cheng PKC**, Wong DA, Tong LKL, Ip S-M, Lo ACT, Lau C-S, Yeung EYH, Lim WWL. 2004. Viral shedding patterns of coronavirus in patients with probable severe acute respiratory syndrome. *The Lancet* **363**:1699–1700. DOI: [https://doi.org/10.1016/S0140-6736\(04\)16255-7](https://doi.org/10.1016/S0140-6736(04)16255-7)
- Chu KH**, Tsang WK, Tang CS, Lam MF, Lai FM, To KF, Fung KS, Tang HL, Yan WW, Chan HW, Lai TS, Tong KL, Lai KN. 2005. Acute renal impairment in coronavirus-associated severe acute respiratory syndrome. *Kidney International* **67**:698–705. DOI: <https://doi.org/10.1111/j.1523-1755.2005.67130.x>, PMID: 15673319
- Daly JL**, Simonetti B, Klein K, Chen KE, Williamson MK, Antón-Plágaro C, Shoemark DK, Simón-Gracia L, Bauer M, Hollandi R, Greber UF, Horvath P, Sessions RB, Helenius A, Hiscox JA, Teesalu T, Matthews DA, Davidson AD, Collins BM, Cullen PJ, et al. 2020. Neuropilin-1 is a host factor for SARS-CoV-2 infection. *Science* **370**:861–865. DOI: <https://doi.org/10.1126/science.abd3072>, PMID: 33082294
- Daniloski Z**, Jordan TX, Wessels H-H, Hoagland DA, Kasela S, Legut M, Maniatis S, Mimitou EP, Lu L, Geller E, Danziger O, Rosenberg BR, Phatnani H, Smibert P, Lappalainen T, tenOever BR, Sanjana NE. 2020. Identification of required host factors for SARS-CoV-2 infection in human cells. *Cell* **8674**:31394. DOI: <https://doi.org/10.1016/j.cell.2020.10.030>
- Drosten C**, Günther S, Preiser W, van der Werf S, Brodt H-R, Becker S, Rabenau H, Panning M, Kolesnikova L, Fouchier RAM, Berger A, Burguière A-M, Cinatl J, Eickmann M, Escriu N, Grywna K, Kramme S, Manuguerra J-C, Müller S, Rickerts V, et al. 2003. Identification of a novel coronavirus in patients with severe acute respiratory syndrome. *New England Journal of Medicine* **348**:1967–1976. DOI: <https://doi.org/10.1056/NEJMoa030747>
- Follis KE**, York J, Nunberg JH. 2006. Furin cleavage of the SARS coronavirus spike glycoprotein enhances cell-cell fusion but does not affect virion entry. *Virology* **350**:358–369. DOI: <https://doi.org/10.1016/j.virol.2006.02.003>, PMID: 16519916
- Gupta A**, Madhavan MV, Sehgal K, Nair N, Mahajan S, Sehrawat TS, Bikdeli B, Ahluwalia N, Ausiello JC, Wan EY, Freedberg DE, Kirtane AJ, Parikh SA, Maurer MS, Nordvig AS, Accili D, Bathon JM, Mohan S, Bauer KA, Leon MB, et al. 2020. Extrapulmonary manifestations of COVID-19. *Nature Medicine* **26**:1017–1032. DOI: <https://doi.org/10.1038/s41591-020-0968-3>, PMID: 32651579
- Hiemstra PS**, Eenjes E, Riet SV, Kroon AA, Slats AM, Reiss IKM, Clevers H, Rottier RJ. 2020. Disease modelling following organoid-based expansion of airway epithelial cells. *European Respiratory Journal* **56**:4322. DOI: <https://doi.org/10.1183/13993003.congress-2020.4322>
- Hoffmann M**, Kleine-Weber H, Pöhlmann S. 2020a. A multibasic cleavage site in the spike protein of SARS-CoV-2 is essential for infection of human lung cells. *Molecular Cell* **78**:779–784. DOI: <https://doi.org/10.1016/j.molcel.2020.04.022>
- Hoffmann M**, Kleine-Weber H, Schroeder S, Krüger N, Herrler T, Erichsen S, Schiergens TS, Herrler G, Wu NH, Nitsche A, Müller MA, Drosten C, Pöhlmann S. 2020b. SARS-CoV-2 cell entry depends on ACE2 and TMPRSS2 and is blocked by a clinically proven protease inhibitor. *Cell* **181**:271–280. DOI: <https://doi.org/10.1016/j.cell.2020.02.052>, PMID: 32142651
- Hoffmann M**, Mösbauer K, Hofmann-Winkler H, Kaul A, Kleine-Weber H, Krüger N, Gassen NC, Müller MA, Drosten C, Pöhlmann S. 2020c. Chloroquine does not inhibit infection of human lung cells with SARS-CoV-2. *Nature* **585**:588–590. DOI: <https://doi.org/10.1038/s41586-020-2575-3>, PMID: 32698190
- Hu B**, Ge X, Wang LF, Shi Z. 2015. Bat origin of human coronaviruses. *Virology Journal* **12**:221. DOI: <https://doi.org/10.1186/s12985-015-0422-1>, PMID: 26689940
- Huang L**, Zhang X, Zhang X, Wei Z, Zhang L, Xu J, Liang P, Xu Y, Zhang C, Xu A. 2020. Rapid asymptomatic transmission of COVID-19 during the incubation period demonstrating strong infectivity in a cluster of youngsters aged 16–23 years outside Wuhan and characteristics of young patients with COVID-19: a prospective contact-tracing study. *Journal of Infection* **80**:e1–e13. DOI: <https://doi.org/10.1016/j.jinf.2020.03.006>
- Hulswit RJ**, de Haan CA, Bosch BJ. 2016. Coronavirus spike protein and tropism changes. *Advances in Virus Research* **96**:29–57. DOI: <https://doi.org/10.1016/bs.aivir.2016.08.004>, PMID: 27712627
- Kimball A**, Hatfield KM, Arons M, James A, Taylor J, Spicer K, Bardossy AC, Oakley LP, Tanwar S, Chisty Z, Bell JM, Methner M, Harney J, Jacobs JR, Carlson CM, McLaughlin HP, Stone N, Clark S, Brostrom-Smith C, Page LC, et al. 2020. Asymptomatic and presymptomatic SARS-CoV-2 infections in residents of a Long-Term care skilled nursing facility - King county, Washington, march 2020. *MMWR. Morbidity and Mortality Weekly Report* **69**:377–381. DOI: <https://doi.org/10.15585/mmwr.mm6913e1>, PMID: 32240128
- Klimstra WB**, Tilston-Lunel NL, Nambulli S, Boslett J, McMillen CM, Gilliland T, Dunn MD, Sun C, Wheeler SE, Wells A. 2020. SARS-CoV-2 growth, furin-cleavage-site adaptation and neutralization using serum from acutely infected, hospitalized COVID-19 patients. *bioRxiv*. DOI: <https://doi.org/10.1101/2020.06.19.154930>
- Kuiken T**, Fouchier RAM, Schutten M, Rimmelzwaan GF, van Amerongen G, van Riel D, Laman JD, de Jong T, van Doornum G, Lim W, Ling AE, Chan PKS, Tam JS, Zambon MC, Gopal R, Drosten C, van der Werf S, Escriu N, Manuguerra J-C, Stöhr K, et al. 2003. Newly discovered coronavirus as the primary cause of severe acute respiratory syndrome. *The Lancet* **362**:263–270. DOI: [https://doi.org/10.1016/S0140-6736\(03\)13967-0](https://doi.org/10.1016/S0140-6736(03)13967-0)
- Lamers MM**, Beumer J, van der Vaart J, Knoops K, Puschhof J, Breugem TI, Ravelli RBG, Paul van Schayck J, Mykityn AZ, Duimel HQ, van Donselaar E, Riesebosch S, Kuijpers HJH, Schipper D, van de Wetering WJ, de

- Graaf M, Koopmans M, Cuppen E, Peters PJ, Haagmans BL, et al. 2020. SARS-CoV-2 productively infects human gut enterocytes. *Science* **369**:50–54. DOI: <https://doi.org/10.1126/science.abc1669>, PMID: 32358202
- Lau SK, Li KS, Huang Y, Shek CT, Tse H, Wang M, Choi GK, Xu H, Lam CS, Guo R, Chan KH, Zheng BJ, Woo PC, Yuen KY. 2010. Ecoepidemiology and complete genome comparison of different strains of severe acute respiratory Syndrome-Related Rhinolphus bat coronavirus in China reveal bats as a reservoir for acute, Self-Limiting infection that allows recombination events. *Journal of Virology* **84**:2808–2819. DOI: <https://doi.org/10.1128/JVI.02219-09>, PMID: 20071579
- Lau SY, Wang P, Mok BW, Zhang AJ, Chu H, Lee AC, Deng S, Chen P, Chan KH, Song W, Chen Z, To KK, Chan JF, Yuen KY, Chen H. 2020. Attenuated SARS-CoV-2 variants with deletions at the S1/S2 junction. *Emerging Microbes & Infections* **9**:837–842. DOI: <https://doi.org/10.1080/22221751.2020.1756700>, PMID: 32301390
- Menachery VD, Dinnon KH, Yount BL, McAnarney ET, Gralinski LE, Hale A, Graham RL, Scobey T, Anthony SJ, Graham B, Randell SH, Lipkin WI, Baric RS, Baric RS. 2020. Trypsin treatment unlocks barrier for zoonotic bat coronavirus infection. *Journal of Virology* **94**:01774-19. DOI: <https://doi.org/10.1128/JVI.01774-19>
- Millet JK, Whittaker GR. 2015. Host cell proteases: critical determinants of coronavirus tropism and pathogenesis. *Virus Research* **202**:120–134. DOI: <https://doi.org/10.1016/j.virusres.2014.11.021>, PMID: 25445340
- Ogando NS, Dalebout TJ, Zevenhoven-Dobbe JC, Limpens R, van der Meer Y, Caly L, Druce J, de Vries JJC, Kikkert M, Bárcena M, Sidorov I, Snijder EJ. 2020. SARS-coronavirus-2 replication in vero E6 cells: replication kinetics, rapid adaptation and cytopathology. *Journal of General Virology* **101**:925–940. DOI: <https://doi.org/10.1099/jgv.0.001453>, PMID: 32568027
- Park JE, Li K, Barlan A, Fehr AR, Perlman S, McCray PB, Gallagher T. 2016. Proteolytic processing of middle east respiratory syndrome coronavirus spikes expands virus tropism. *PNAS* **113**:12262–12267. DOI: <https://doi.org/10.1073/pnas.1608147113>, PMID: 27791014
- Peiris JSM, Chu CM, Cheng VCC, Chan KS, Hung IFN, Poon LLM, Law KI, Tang BSF, Hon TYW, Chan CS, Chan KH, Ng JSC, Zheng BJ, Ng WL, Lai RWM, Guan Y, Yuen KY. 2003a. Clinical progression and viral load in a community outbreak of coronavirus-associated SARS pneumonia: a prospective study. *The Lancet* **361**:1767–1772. DOI: [https://doi.org/10.1016/S0140-6736\(03\)13412-5](https://doi.org/10.1016/S0140-6736(03)13412-5)
- Peiris JSM, Lai ST, Poon LLM, Guan Y, Yam LYC, Lim WY, Nicholls J, Yee WKS, Yan WW, Cheung MT, Cheng VCC, Chan KH, Tsang DNC, Yung RWH, Ng TK, Yuen KY. 2003b. Coronavirus as a possible cause of severe acute respiratory syndrome. *The Lancet* **361**:1319–1325. DOI: [https://doi.org/10.1016/S0140-6736\(03\)13077-2](https://doi.org/10.1016/S0140-6736(03)13077-2)
- Rockx B, Kuiken T, Herfst S, Bestebroer T, Lamers MM, Oude Munnink BB, de Meulder D, van Amerongen G, van den Brand J, Okba NMA, Schipper D, van Run P, Leijten L, Sikkema R, Verschoor E, Verstrepen B, Bogers W, Langermans J, Drosten C, Fentener van Vlissingen M, et al. 2020. Comparative pathogenesis of COVID-19, MERS, and SARS in a nonhuman primate model. *Science* **368**:1012–1015. DOI: <https://doi.org/10.1126/science.abb7314>, PMID: 32303590
- Sachs N, Papaspyropoulos A, Zomer-van Ommen DD, Heo I, Böttinger L, Klay D, Weeber F, Huelsz-Prince G, Iakobachvili N, Amatngalim GD, Ligt J, Hoeck A, Proost N, Viveen MC, Lyubimova A, Teeven L, Derakhshan S, Korving J, Begthel H, Dekkers JF, et al. 2019. Long-term expanding human airway organoids for disease modeling. *The EMBO Journal* **38**:2018100300. DOI: <https://doi.org/10.15252/embj.2018100300>
- Shang J, Wan Y, Luo C, Ye G, Geng Q, Auerbach A, Li F. 2020. Cell entry mechanisms of SARS-CoV-2. *PNAS* **117**:11727–11734. DOI: <https://doi.org/10.1073/pnas.2003138117>, PMID: 32376634
- Vincent MJ, Bergeron E, Benjannet S, Erickson BR, Rollin PE, Ksiazek TG, Seidah NG, Nichol ST. 2005. Chloroquine is a potent inhibitor of SARS coronavirus infection and spread. *Virology Journal* **2**:69. DOI: <https://doi.org/10.1186/1743-422X-2-69>, PMID: 16115318
- Walls AC, Park Y-J, Tortorici MA, Wall A, McGuire AT, Veasley D. 2020. Structure, function, and antigenicity of the SARS-CoV-2 spike glycoprotein. *Cell* **181**:281–292. DOI: <https://doi.org/10.1016/j.cell.2020.02.058>
- Wang Q, Qi J, Yuan Y, Xuan Y, Han P, Wan Y, Ji W, Li Y, Wu Y, Wang J, Iwamoto A, Woo PC, Yuen KY, Yan J, Lu G, Gao GF. 2014. Bat origins of MERS-CoV supported by bat coronavirus HKU4 usage of human receptor CD26. *Cell Host & Microbe* **16**:328–337. DOI: <https://doi.org/10.1016/j.chom.2014.08.009>, PMID: 25211075
- Wang M, Cao R, Zhang L, Yang X, Liu J, Xu M, Shi Z, Hu Z, Zhong W, Xiao G. 2020. Remdesivir and chloroquine effectively inhibit the recently emerged novel coronavirus (2019-nCoV) in vitro. *Cell Research* **30**:269–271. DOI: <https://doi.org/10.1038/s41422-020-0282-0>, PMID: 32020029
- Wei J, Alfajaro MM, Hanna RE, DeWeirdt PC, Strine MS, Lu-Culligan WJ, Zhang SM, Graziano VR, Schmitz CO, Chen JS. 2020a. Genome-wide CRISPR screen reveals host genes that regulate SARS-CoV-2 infection. *bioRxiv*. DOI: <https://doi.org/10.1101/2020.06.16.155101>
- Wei WE, Li Z, Chiew CJ, Yong SE, Toh MP, Lee VJ. 2020b. Presymptomatic transmission of SARS-CoV-2 - Singapore, January 23-March 16, 2020. *MMWR. Morbidity and Mortality Weekly Report* **69**:411–415. DOI: <https://doi.org/10.15585/mmwr.mm6914e1>, PMID: 32271722
- Whelan SP, Ball LA, Barr JN, Wertz GT. 1995. Efficient recovery of infectious vesicular stomatitis virus entirely from cDNA clones. *PNAS* **92**:8388–8392. DOI: <https://doi.org/10.1073/pnas.92.18.8388>, PMID: 7667300
- Wiersinga WJ, Rhodes A, Cheng AC, Peacock SJ, Prescott HC. 2020. Pathophysiology, transmission, diagnosis, and treatment of coronavirus disease 2019 (COVID-19): A review. *JAMA* **324**:782. DOI: <https://doi.org/10.1001/jama.2020.12839>, PMID: 32648899
- Wrapp D, Wang N, Corbett KS, Goldsmith JA, Hsieh CL, Abiona O, Graham BS, McLellan JS. 2020. Cryo-EM structure of the 2019-nCoV spike in the prefusion conformation. *Science* **367**:1260–1263. DOI: <https://doi.org/10.1126/science.abb2507>, PMID: 32075877

- Wrobel AG**, Benton DJ, Xu P, Roustan C, Martin SR, Rosenthal PB, Skehel JJ, Gamblin SJ. 2020. SARS-CoV-2 and bat RaTG13 spike glycoprotein structures inform on virus evolution and furin-cleavage effects. *Nature Structural & Molecular Biology* **27**:0468-7. DOI: <https://doi.org/10.1038/s41594-020-0468-7>
- Yang Y**, Du L, Liu C, Wang L, Ma C, Tang J, Baric RS, Jiang S, Li F. 2014. Receptor usage and cell entry of bat coronavirus HKU4 provide insight into bat-to-human transmission of MERS coronavirus. *PNAS* **111**:12516–12521. DOI: <https://doi.org/10.1073/pnas.1405889111>, PMID: 25114257
- Yang Y**, Liu C, Du L, Jiang S, Shi Z, Baric RS, Li F. 2015. Two mutations were critical for Bat-to-Human transmission of middle east respiratory syndrome coronavirus. *Journal of Virology* **89**:9119–9123. DOI: <https://doi.org/10.1128/JVI.01279-15>, PMID: 26063432
- Zaki AM**, van Boheemen S, Bestebroer TM, Osterhaus ADME, Fouchier RAM. 2012. Isolation of a novel coronavirus from a man with pneumonia in Saudi Arabia. *New England Journal of Medicine* **367**:1814–1820. DOI: <https://doi.org/10.1056/NEJMoa1211721>
- Zhou Y**, Vedantham P, Lu K, Agudelo J, Carrion R, Nunneley JW, Barnard D, Pöhlmann S, McKerrow JH, Renslo AR, Simmons G. 2015. Protease inhibitors targeting coronavirus and filovirus entry. *Antiviral Research* **116**:76–84. DOI: <https://doi.org/10.1016/j.antiviral.2015.01.011>
- Zhu N**, Zhang D, Wang W, Li X, Yang B, Song J, Zhao X, Huang B, Shi W, Lu R, Niu P, Zhan F, Ma X, Wang D, Xu W, Wu G, Gao GF, Tan W. 2020. A novel coronavirus from patients with pneumonia in China, 2019. *New England Journal of Medicine* **382**:727–733. DOI: <https://doi.org/10.1056/NEJMoa2001017>